



Pulsed neutron-beam flux with the supermirror neutron guide system at AISTANS

Koichi Kino^{1,2,a} , Michihiro Furusaka^{1,2} , Takeshi Fujiwara^{1,2} , Brian E. O'Rourke^{1,2} , Takemi Muroga²,
Yo Tomota^{1,2} , Nagayasu Oshima^{1,2} 

¹ National Institute of Advanced Industrial Science and Technology (AIST), Tsukuba, Ibaraki, Japan

² Innovative Structural Materials Association (ISMA), Chiyoda-Ku, Tokyo, Japan

Received: 15 May 2022 / Accepted: 8 October 2022

© The Author(s), under exclusive licence to Società Italiana di Fisica and Springer-Verlag GmbH Germany, part of Springer Nature 2022

Abstract Neutron-beam flux spectra at the compact electron accelerator-driven pulsed neutron facility AISTANS were measured at a detector position of 8 m from the neutron source. Based on the measured spectra, the characteristics of the neutron beam from the decoupled ~20 K solid methane moderator and the amplification of the neutron-beam flux at the detector position when supermirror guide tubes are installed in the beamline between the moderator and detector position were analyzed. A neutron spectral temperature of 32.6 K was observed, suggesting a physical temperature for the moderator of roughly 26 K with an electron beam power on a neutron production target of ~1 kW. Furthermore, the absolute intensity of the measurement spectrum was of the same order (approximately 2/3) as that of the simulation calculation. The geometrical neutron path and neutron phase space through the supermirror guide tubes were investigated diagrammatically to find the relationship between the neutron reflection position and wavelength and measured imaging quality. The increase in neutron flux at the detector when supermirror guide tubes are used was measured experimentally, and the results showed reasonable agreements with those of the simulation calculations. This amplification factor reached a value of approximately 6 at a wavelength of around 0.4 nm and approximately 8 for the long neutron wavelength exceeding 0.7 nm.

1 Introduction

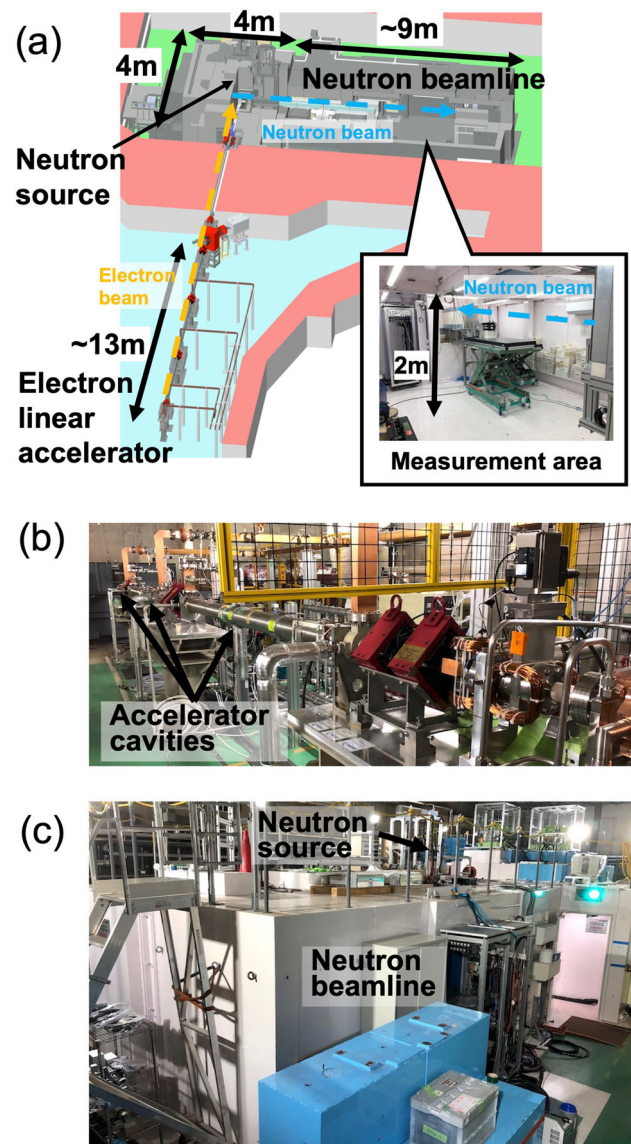
Accelerator-driven pulsed neutron sources are actively used in material science and industry. Large-scale pulsed neutron sources based on the spallation reaction are available, such as the Japan spallation neutron source (JSNS) at the Japan Proton Accelerator Research Complex (J-PARC) in Japan [1], the spallation neutron source (SNS) at Oak Ridge National Laboratory (ORNL) in the USA [2], ISIS at the Rutherford Appleton Laboratory (RAL) in the UK [3], and the China spallation neutron source (CSNS) at the Institute of High Energy Physics (IHEP) in China [4]. In Sweden, the European spallation source (ESS) is under construction [5].

In addition to these spallation sources, measurement facilities based on compact accelerator-driven neutron sources (CANS) have also been actively developed. The worldwide collaboration named 'Union for Compact Accelerator-driven Neutron Sources' (UCANS) [6, 7] was formed in 2010 and supports the spread of CANS. There are operating many CANS facilities such as Bariloche LINAC in Argentina [8], GELINA in Belgium [9], CPHS in China [10], SARAF in Israel [11], Pohang Neutron Facility in South Korea [12] and so on. The world's CANS facilities in operation and under development are summarized in a recent review [13] and on the IAEA website [14]. In Japan, the Japan collaboration on accelerator-driven neutron sources (JCANS) [15, 16] has many active facilities, including the Hokkaido University neutron source (HUNS) [17], the RIKEN accelerator-driven compact neutron source (RANS) [18], and the recently developed analytical facility for industrial science and technology using accelerator-based neutron source (AISTANS) [19, 20], which is the subject of this study. These facilities provide incident (electron or proton) beams with arbitrary repetition rates and pulse widths for a single target, moderator, and reflector (TMR) system, in contrast to the HBS [21–23] and SONATE [24] projects in Europe, where some incident proton beams with different repetition rates and pulse widths are provided to each TMR system suitable for different neutron measurement instruments.

The advantage of the accelerator-based pulsed neutron source is that data can be acquired over a wide neutron wavelength range simultaneously using a pulsed neutron beam, in contrast to the use of a monochromatic neutron beam. Pulsed neutron beams are used in various measurement methods and are particularly useful for Bragg-edge imaging. This imaging technique is a neutron transmission measurement when the Bragg condition can be satisfied as a function of wavelength, on a beamline with sufficient collimation to allow imaging. Wavelength-resolved images are easily obtained using the time-of-flight method [25]. This imaging technique enables to determine various crystallographic information as images, and has been widely used in the analysis of various samples including steel products and historical artifacts [26].

^a e-mail: koichi.kino@aist.go.jp (corresponding author)

Fig. 1 Overview of AISTANS. **(a)** Cut-away 3D model showing the electron linear accelerator, neutron source, and neutron beamline. The measurement area is inside the neutron beamline hutch and is around 8 m from the neutron source. **(b)** Photograph of the electron linear accelerator with the electron gun in the foreground and electrons accelerated through the accelerator cavities toward the neutron production target located beyond the concrete shielding wall. **(c)** Photograph of the neutron source (blue color) and the neutron beamline (cream color). Staff operating the facility can remain in this room (outside of the neutron beamline hutch) during operation



AISTANS, which is a newly developed CANS at the National Institute of Advanced Industrial Science and Technology (AIST) in Japan, is optimized for Bragg-edge imaging and can be used to aid the development of structural materials for transportation vehicles [19, 20]. AISTANS is composed of an electron linear accelerator with a length of ~ 13 m, a neutron source with an area of approximately 4×4 m, and a ~ 9 m long neutron beamline as shown in Fig. 1. The compact size of AISTANS enables relatively straightforward operation, maintenance, and machine time scheduling compared to large facilities, and all operations can be performed by a research group consisting of several people. Therefore, flexible operations suitable for industrial requirements are possible. However, the neutron production rate of a CANS is much lower than that of large facilities; for example, that of AISTANS is approximately 10^{-5} times that of J-PARC. To overcome this disadvantage and make it possible to obtain statistically sufficient data within a reasonable measurement time required for industrial requirements, various strategies have been adopted at the AISTANS. An example is the use of supermirror guide tubes in the neutron beamline to improve the neutron transport efficiency [19]. Supermirror guide tubes are neutron reflection devices made of multilayers of Ni and Ti on a substrate such as glass.

There are two trends of using a supermirror guide tubes in wavelength-resolved imaging, including Bragg-edge imaging, beamlines at pulsed neutron-beam facilities. Supermirror guide tubes are not used in J-PARC RADEN [27] or SNS VENUS [28]. At these beamlines, a pulsed neutron beam with a narrow time width and high intensity is used with a flight path length of 18–25 m. However, supermirror guide tubes are used at the ISIS IMAT [29] and ESS ODIN [30, 31]. At these beamlines, the flight path lengths are 56 m and 60 m, respectively, which are relatively longer than those of RADEN and VENUS. At IMAT, a pulsed neutron beam from a coupled moderator, whose time pulse is wider than those of RADEN and VENUS, is used. At ODIN, the pulsed neutron beam from the butterfly moderator [32] for the long pulse design at the ESS is used with a built-in neutron-beam chopper system. At IMAT and

ODIN, the supermirror guide tubes end 10 m upstream from the sample position, and this 10 m free space is useful in obtaining the required measurement field with an appropriate beam divergence.

Contrary to the beamlines at large facilities, no beamline at a CANS has permanent supermirror guide tubes installed for wavelength resolved imaging. Supermirror guide tubes should be used actively used in CANS because their neutron intensity is relatively low. At HUNS, the combination of an existing supermirror guide tube and a 300-K polyethylene decoupled moderator was demonstrated [33, 34]. However, at AISTANS, a decoupled 20 K solid methane moderator closely coupled with supermirror guide tubes was adopted from the beginning of the grand design [19]. This design delivers intense, short pulse neutron beams at low neutron energy (thermal to cold neutrons), which is impossible using a 300 K polyethylene moderator, by using a decoupled ~20 K solid methane moderator. The guide efficiency is larger for lower-energy (longer-wavelength) neutrons because the critical angle of neutron reflection at the supermirror guide tubes is proportional to the neutron wavelength [35]. Furthermore, it is much easier to install optical devices such as supermirror guide tubes tightly coupled to the neutron sources, at a CANS facility because radiation damage is much lower compared with high-power spallation neutron sources [21, 36]. At AISTANS, the introduction of the supermirror guide tubes is only 651 mm from the moderator compared with 1.5~2 m for large facilities; hence, large phase-space of neutrons are available.

This paper reports on research conducted at AISTANS with the aim of clarifying the neutron flux amplification effect/usefulness of supermirror guide tubes in CANS. In this study, the neutron-beam flux was experimentally measured in different supermirror guide tube configurations. These measurements were compared with each other and evaluated using Monte Carlo simulations, geometric/topological analysis of neutron trajectories. Note that in this paper neutron flux is a function of neutron wavelength.

The structure of this paper is as follows. In Sect. 2, experimental methods are described. In Sect. 3, the analysis of experimental data is described. In order to accurately extract the transport efficiency of the guide tubes, the measured data are processed/corrected according to various aspects. For example, the measured flux data were corrected by removing the effects of neutron absorption and scattering by metal parts and air on the beamline including the moderator vessel. In addition, the flux data were also corrected by Monte Carlo simulation related to the TMR system including the injection spot size of an electron beam at the neutron production target so that the flux data can be normalized by the electron beam irradiation power. In Sect. 4, the results and discussion are presented, which is divided into three subsections for different analytical points of view. In Sect. 4.1, we evaluate the absolute value of the neutron-beam flux emitted from a solid methane moderator without the supermirror guide tubes. In Sect. 4.2, the geometry and phase space of the neutron trajectories from the moderator surface to the detector position are discussed to diagrammatically reveal the properties of the guide tubes including amplification effect and beam divergence angle. Also, the effects of transmission imaging blurring caused by the beam divergence angle are discussed. In Sect. 4.3, the beam flux amplification effect is evaluated based on Monte Carlo simulation calculations. In Sect. 5, the conclusions of this study are described.

2 Experimental

Fast neutrons were produced in a tantalum target which is irradiated by an electron beam provided by the electron linear accelerator. The target consisted of many thin plates of tantalum with a cross section of 50 (W) × 50 mm (H) stacked perpendicular to the beam direction, cooled by water, and covered by a titanium housing with dimensions of 90 (W) × 60 (H) × 108 mm (D). There were two cooling water channels along the sides of the tantalum plate. Its detailed drawing is given in the reference 19.

A decoupled solid methane moderator with dimensions of 12 (W) × 12 (H) × 3 cm (D) was placed above the target, and a coupled solid methane moderator with dimensions of 12 (W) × 12 (H) × 5 cm (D) was placed below the target that will be used in the near future for a second beamline. The material of the inner reflector was graphite, and lead was used for the outer reflector and gamma-ray shielding. The aluminum moderator vessel was cooled by circulating helium-gas at ~20 K, and the methane gas was liquefied and then solidified by circulating helium gas. The TMR was placed in a helium vessel.

The neutron flux was measured at a distance of 8 m from the decoupled solid methane moderator in the beamline hutch. There were three sections of supermirror guide tubes between the moderator and the detector, as shown in Fig. 2, and the second and third guide tube sections at the beam downstream can be exchanged with a vacuum chamber with a much larger cross section without supermirror guide tubes. If the second and third guide tube sections are used with the first one, a relatively bright beam can be obtained in a relatively small area (approximately 100 × 100 mm) at the sample position. However, if the second and third guide tubes are not used (eliminated from the beamline axis), a relatively low-brightness beam can be provided in a relatively large area (approximately 300 × 300 mm) at the sample position.

The most upstream guide tube, “first section”, was installed in the beam shutter at 651 mm from the moderator center and was 970 mm long with a cross section of 130 × 130 mm. However, this section could not be eliminated from the beamline. The second guide tube section follows the first section with a total length of 1715 mm and a cross section of 130 × 130 mm. The third section was 2000 mm long with a cross section of 123 × 123 mm. There were small gaps between the second and third sections for installation of the neutron wavelength-band chopper, which will be explained later. The cross sections of the guide tubes were determined to obtain an approximately 100 × 100 mm beam spot at a sample position of 8 m. The slightly smaller cross section of the third section compared to that of the second section compensates for the neutron transportation loss owing to the small gaps. With this treatment, the gaps optically disappeared when viewed from the beamline center at the sample position. The guide tubes were evacuated to a vacuum using a dry scroll pump. After the beam shutter, a selectable pinhole exchanger system was installed, which

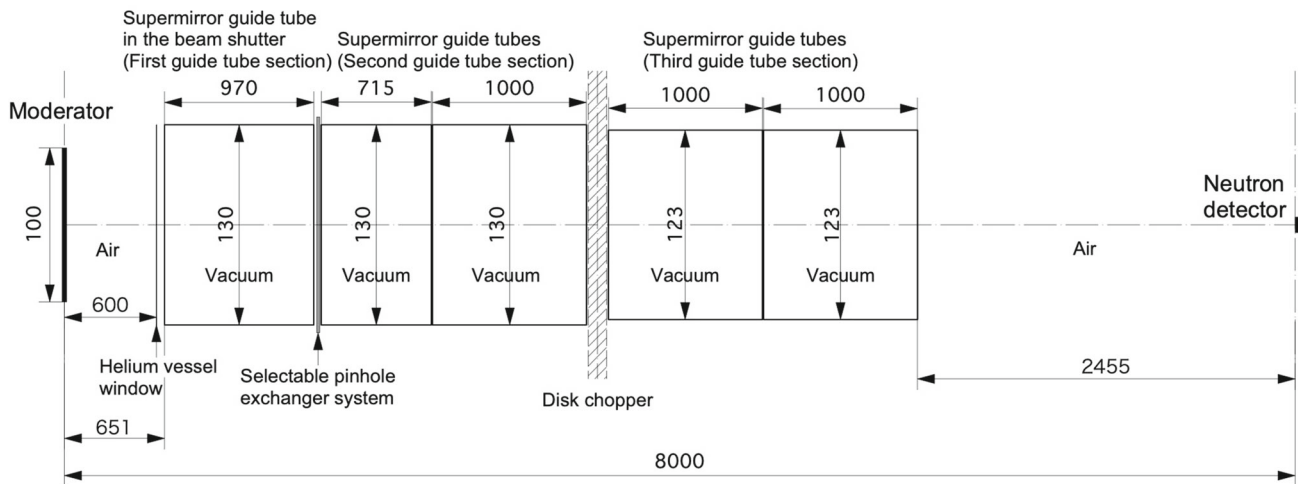


Fig. 2 Neutron flux measurement system (units in mm). The distance between the neutron moderator and the neutron detector is 8.0 m. There are three sections of supermirror guide tubes between the moderator and the detector. The second and third guide tube sections can be easily removed and the flux measurements are performed for the three settings of the supermirror guide tubes summarized in Table 1

Table 1 Supermirror guide tube sections used in the three measurement settings

Setting	Supermirror guide tube		
	First section	Second section	Third section
1	IN	IN	IN
2	IN	IN	OUT
3	IN	OUT	OUT

could reduce the beam to 10, 20, 40, and 80-mm diameters or 130×130 mm to control the neutron-beam divergence. For the present measurements, a 130×130 mm hole was used. Between the second and the third guide/vacuum tubes, a neutron wavelength-band chopper was installed to eliminate frame-overlapped neutrons. The beam chopper is composed of 2 counter-rotating disk chopper blades with a radius of 370 mm, rotating at a maximum of 25 Hz with four beam-passing windows, each having a 57° opening angle. However, for this measurement, the disk chopper was stopped in the beam-passing position to obtain neutron spectra in a wider neutron wavelength range. A ^3He proportional neutron counter of diameter 25.4 mm and covered by a cadmium sheet with a 1 cm^2 aperture was placed on the beamline axis 8 m from the moderator.

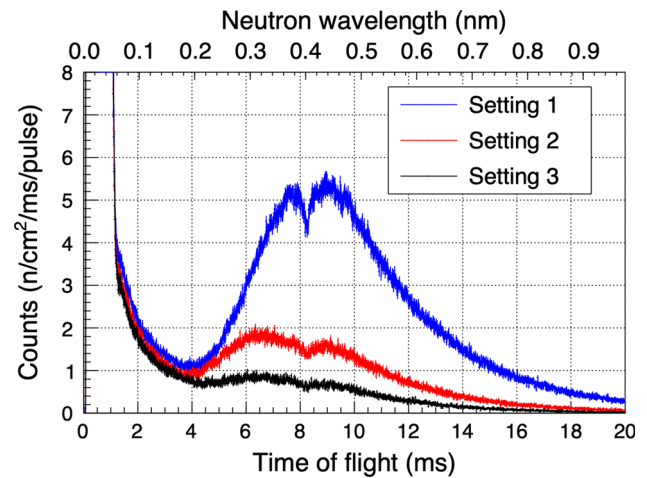
We conducted three sets of measurements under the conditions listed in Table 1 to check the properties of the neutron beam emitted from the moderator and the effect of the supermirror guide tubes. Three different settings were used; Setting 1, all supermirror guide tubes (first, second and third sections) were inserted into the beamline; Setting 2, first and second sections installed (third section removed) and Setting 3, only the first section installed. Vacuum tubes were not installed during the measurements, therefore, the neutron beam passed through air when the guide tubes were removed from the neutron beamline. The repetition rate, energy, peak current, and pulse width of the electron beam were 50 Hz, ~ 40 MeV, 120 mA, and 4 μs , respectively, at the end of the electron linear accelerator. This corresponded to an average beam power of approximately 1 kW. The peak electron beam current on the neutron production target, including the target housing, was measured using the Faraday cup method, and it was approximately 100 mA with a pulse width of 4 μs . The peak current measured at the target was lower than that measured in the accelerator because of the scattering of the electron beam by the titanium window at the end of the accelerator vacuum pipe and further scattering in the air between the window and the target. Air will be replaced by helium gas in the future to reduce electron beam loss.

3 Data analysis

3.1 Time of flight calibration

The calibration of the time-of-flight (TOF) was performed using the Bragg-edge cutoff data of the 110, 200, and 211 reflections with a 10-mm-thick steel sample set in front of the neutron detector. We used the relation between the TOF values and the neutron wavelengths (0.405, 0.287, and 0.234 nm) of the cutoffs for these Bragg edges. Figure 3 shows the time-calibrated raw TOF spectra for the three measurement conditions. The broad cold neutron maxima were detected at approximately 6–10 ms, which corresponded to 0.3–0.5 nm wavelength neutrons, and these spectra show different shapes. The neutron counts were significantly

Fig. 3 Calibrated neutron TOF spectra measured at the three different measurement conditions. The maximum TOF is 20 ms because the neutron-beam repetition rate was 50 Hz. The upper horizontal axis is the neutron wavelength corresponding to the TOF



high below ~ 1.2 ms because neutrons with an epithermal energy (above ~ 0.24 eV and wavelength below ~ 0.58 nm) pass through the cadmium window in front of the neutron detector. They were not used in the subsequent analyses.

3.2 Frame overlaps of time-of-flight spectra

The time frame of the TOF was 20 ms, which corresponds to the time interval between successive neutron pulses at a repetition-rate of 50 Hz. Therefore, there were frame overlaps of slow neutrons when the TOF exceeded 20 ms. We estimated the frame overlap contributions as shown in Fig. 4(a) and subtracted them from the TOF spectra using the following procedure. The long flight time tail region of the TOF spectra, ranging from 17 to 20 ms, were fit by a Maxwellian distribution function in the low-energy limit, and the results are shown as green solid curves, considering the attenuation of the neutrons by the beamline materials (aluminum windows and air) as a function of the TOF. In this region, the theoretical neutron spectrum per unit energy derived from the Maxwellian distribution was proportional to the neutron energy. The spectrum per unit TOF, which is expressed in Fig. 4(a), is proportional to t^{-5} , using the TOF time t . The green dashed curves are the estimated frame overlapped neutron spectra, which are extrapolated by the solid lines, displaced by the time corresponding to the electron-beam pulse interval. Although the intensities of these frame-overlap neutrons were relatively low, they were subtracted from the spectra in Fig. 3 to obtain the spectrum shown in Fig. 4(b).

3.3 Neutron detection efficiency

The neutron detector is composed of a 0.5-mm-thick stainless-steel tube and ^3He gas. The measured spectra were then corrected for wavelength-dependent neutron detection efficiency of the neutron detector. The efficiency was calculated using the $^3\text{He}(n,p)^3\text{H}$ reaction cross section, and the thickness (24.4 mm) and pressure (8 atm) of ^3He gas in the detector. Reduction of neutron detection efficiency due to scattering and absorption in the stainless-steel tube wall was considered using the total cross section spectrum calculated using the RITS code [37]. In the calculation, the three main constituents of stainless steel, Fe (74 mass%), Ni (8 mass%), and Cr (18 mass%), were considered and an isotropic crystalline orientation was assumed. The time structure of the neutron pulse estimated previously by Monte Carlo simulation [19] was convoluted to the total cross-section spectrum. The obtained detection efficiency as a function of the neutron wavelength is shown in Fig. 5. The stepped structures observed between ~ 0.2 and ~ 0.43 nm were owing to the Bragg edges of the stainless steel. In the long-wavelength region above ~ 0.43 nm, the efficiency gradually decreased as the wavelength increased because of neutron absorption in the stainless steel. However, the efficiency dropped drastically as the neutron wavelength became shorter, because the $^3\text{He}(n,p)^3\text{H}$ cross section is inversely proportional to the neutron velocity. The estimated neutron flux on the detector was then obtained by convoluting the measured spectra with the calculated neutron detection efficiency of the detector. These estimated flux spectra are shown in Fig. 6 and represent an estimate of the actual neutron fluxes at the detector position obtained under the experimental conditions in the AISTANS. The flux spectra in Fig. 6 vary depending on the neutron wavelength. Therefore, we calculated the average values of the neutron flux between 0.2 and 0.5 nm for setting 1, 2, and 3 and found to be 81.8, 32.6, and 15.7 $\text{n/cm}^2/\text{nm}/\text{pulse}$, respectively. From the viewpoint of the averaged intensity defined here, it was concluded that setting 1 had a transport effect more than 5 times that of setting 3.

3.4 Attenuation of neutrons by aluminum and air

The attenuation of the neutron beam owing to the aluminum moderator vessel, aluminum moderator vacuum chamber, aluminum windows, and air between the moderator and detector were considered for the experimentally obtained data to compare the measured neutron intensity with the simulation calculations. The thicknesses of the moderator vessel and vacuum chamber were 7 and 10 mm,

Fig. 4 Elimination of the frame overlaps in TOF spectra. (a) Estimation of the frame overlaps for the three spectra. The solid lines are the fit curves, and the dashed lines are the estimated frame overlaps. (b) Flux spectra after the frame overlaps subtractions

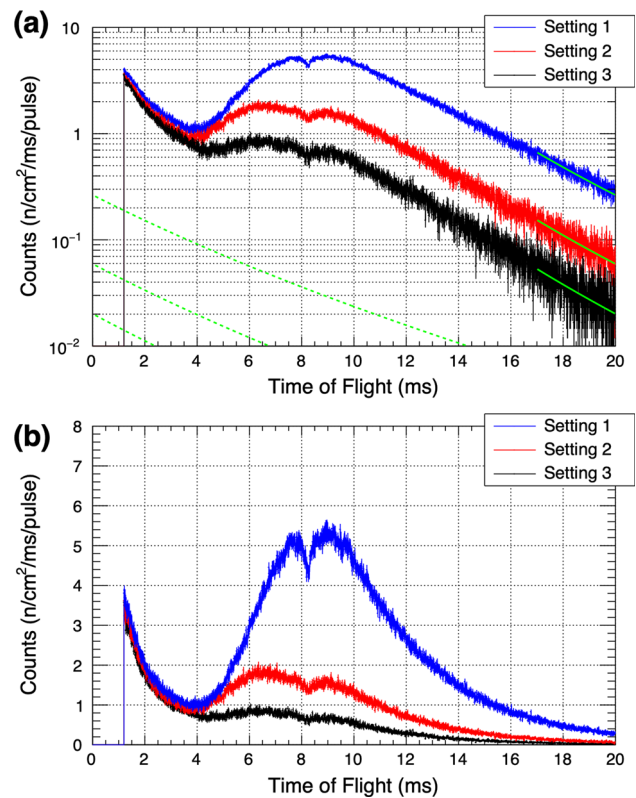
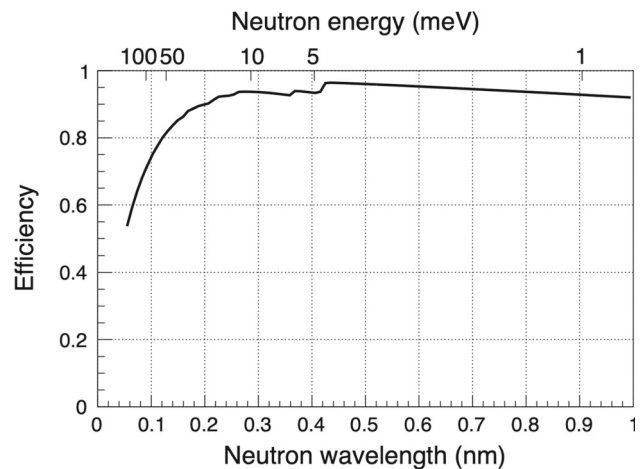


Fig. 5 Neutron detection efficiency of the neutron detector as a function of the neutron wavelength. This efficiency is calculated using the amount of ³He gas in the detector and the neutron attenuation by the cylindrical wall of the detector which is made of stainless-steel



respectively. There were several aluminum windows, including the 3-mm-thick helium-vessel window, which was located 600 mm downstream of the moderator. The vessel was filled with air instead of He at the time of measurements. The other windows were caps at both ends of the supermirror guide tubes with thicknesses of 1.2 or 0.5 mm. The transmission spectra of all the aluminum along the beamline at settings 1, 2, and 3 are shown by dotted lines in Fig. 7. The aluminum total cross section contributed to the neutron attenuation, which was calculated by the code RITS [37], was used to obtain transmission spectra, considering a total thickness of 26.4, 24.4, and 22.4 mm for settings 1, 2, and 3, respectively. In the calculation, the texture was assumed to have the following equal-amount two components according to the intense 200-reflection Bragg edge observed at AISTANS using aluminum plate samples; one component was texture-free, and the other was the preferred orientation of $\langle 100 \rangle$ parallel to the neutron-beam direction. The intense dips at 0.47 nm and 0.40 nm were owing to Bragg edges of 111 and 200 reflections.

The transmission spectra of air shown in Fig. 7 by dashed lines were calculated using the 300 K total cross sections of the nuclear data library JENDL-4.0 [38]. Three atoms, nitrogen, oxygen, and argon, were considered. The solid lines in Fig. 7 show the total attenuation caused by the aluminum and air.

Fig. 6 Estimated neutron flux on the detector as a function of neutron wavelength for the three different measurement settings. The estimated spectra are obtained by convoluting the measured spectra with the neutron detection efficiency of the detector. These spectra represent actual neutron flux estimates at the detector position obtained using AISTANS under the experimental conditions in which the electron accelerator was operated with power of ~ 1 kW and repetition rate of 50 Hz

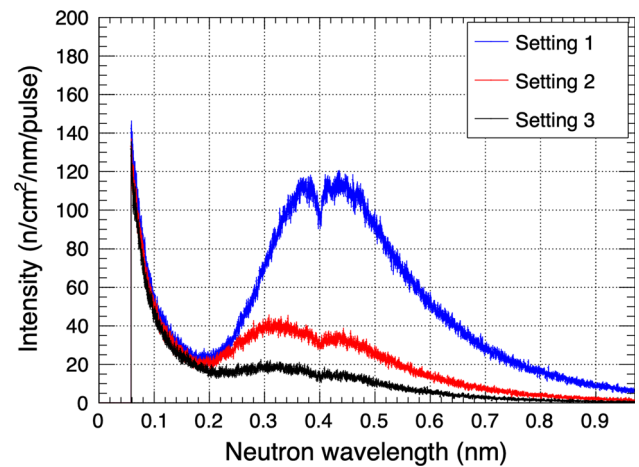
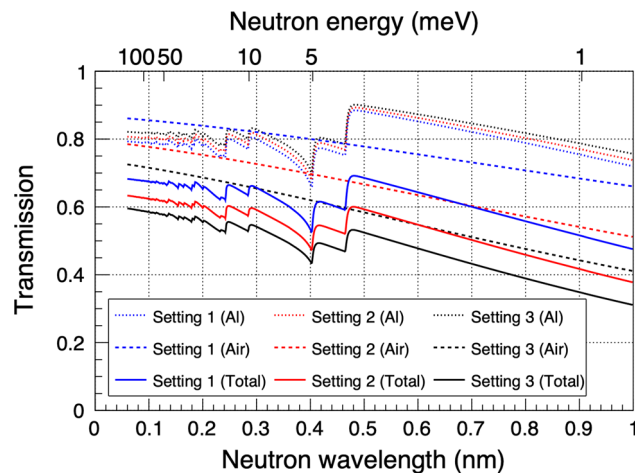


Fig. 7 Calculated transmission spectra of aluminum, air, and their combinations at settings 1, 2, and 3. The aluminum transmission spectra were calculated considering the crystalline orientation on the basis of Bragg-edge measurements of aluminum samples at AISTANS. The air transmission spectra were calculated using the nuclear data library



3.5 Spatial distribution of the electron beam at the neutron production target

As described in Sect. 2, the peak electron beam current of the neutron production target, including its housing, was measured using the Faraday cup method. It was necessary to evaluate the number of electrons incident on the Ta plates in the target housing to compare the measured neutron-beam intensity with simulation calculations. At AISTANS, the electron beam was spatially distributed at the neutron production target, because of the electron beam scattering in the 1.4-m-thick layer of air between the end of the accelerator vacuum duct and the neutron production target and the 30- μm -thick titanium window at the end of the accelerator vacuum duct. Neutrons were primarily produced in the 50 (W) \times 50 mm (H) Ta plates in a 90 (W) \times 60 mm (H) Ti vessel, although we could only measure the number of electrons incident on the Ti vessel surface. The electron beam distribution at the target surface was calculated using the Monte Carlo code PHITS Ver.3.02 [39], assuming a 20-mm diameter, uniformly distributed electron beam from the accelerator. In Fig. 8(a), the projected position of the Ta plates is shown by the area outlined by the red dashed line and that of the target housing by the green dashed line. Figure 8(b) shows the distributions of electrons projected on the horizontal axis. Based on this simulation, the percentage of electrons incident on the tantalum area with respect to the entire target housing was estimated to be 0.75. In the future, the air in the helium vessel will be replaced by helium gas, and the calculated percentage will increase to 0.92.

3.6 Simulation calculation of the neutron beam and supermirror guide tubes

Simulation calculations were performed to discuss the experimentally obtained neutron spectrum as a function of neutron energy and the effect of the supermirror guide tubes. For the neutrons emitted from the moderator, the simulation calculation reported in our previous study [19] was used, but the attenuation of the neutrons through the aluminum moderator vessel and aluminum vacuum chamber for the moderator were included in the previous simulation calculation results. Therefore, these attenuation effects were subtracted using the cross-sectional data adopted in the PHITS Ver.3.02 [39].

The effect of the supermirror guide tubes was calculated using PHITS Ver.3.02 [39], for the three experimental settings with the geometry of the supermirror guide tubes shown in Fig. 2. In this beam transport simulation, a neutron beam from the moderator with

Fig. 8 Spatial distribution of electron beam at the neutron production target. (a) Two-dimensional distribution of electron beam at the target position was calculated by the PHITS Monte Carlo code. The areas inside the dashed green and red lines indicate the target housing and tantalum areas in the target, respectively. (b) Projection of Fig. 8(a) on the X-axis. The distributions for all, target, and tantalum areas are colored by black, green, and red, respectively

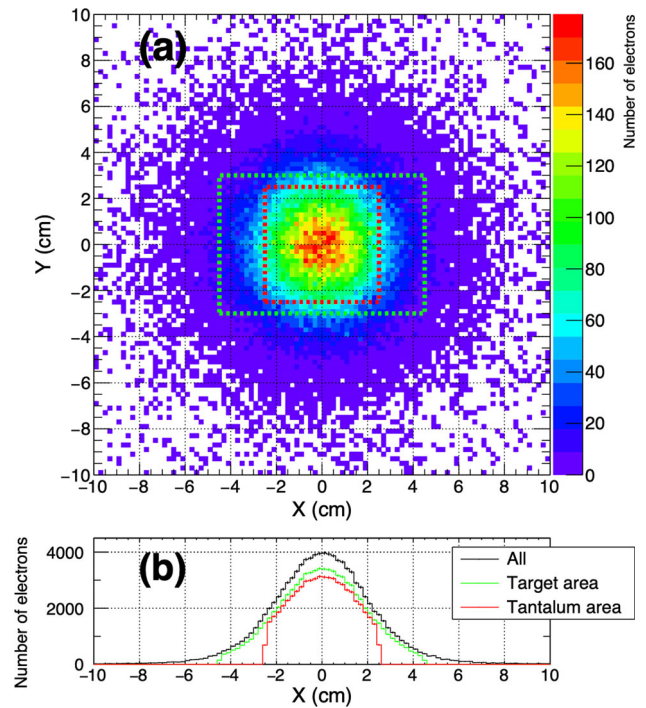
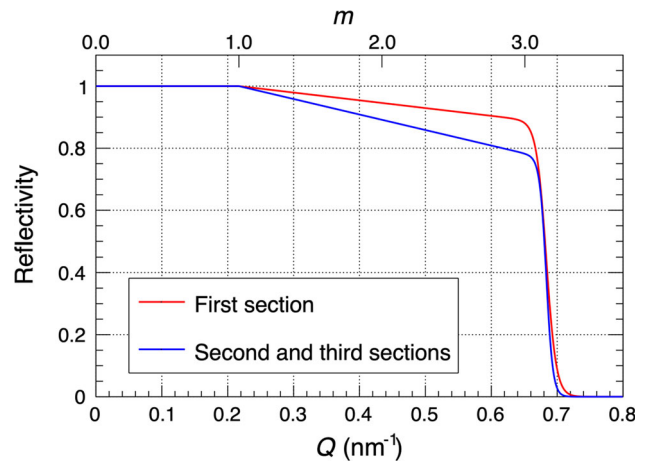


Fig. 9 Reflectivity of the supermirror guide tubes as a function of the scattering vector Q and m -value. These curves are the function of Eq. (1), and the parameters of this equation are summarized in Table 2



previously calculated parameters [19] was incident on the supermirror guide tubes and detected in a 10×10 mm area centered on the beamline axis at a distance of 8.0 m from the moderator. The reflection data of the supermirror guide tubes, which were certified by the manufacturers, were used for each tube section in the calculations. The reflection performances were considered using the following function incorporated in PHITS Ver.3.02 [39]:

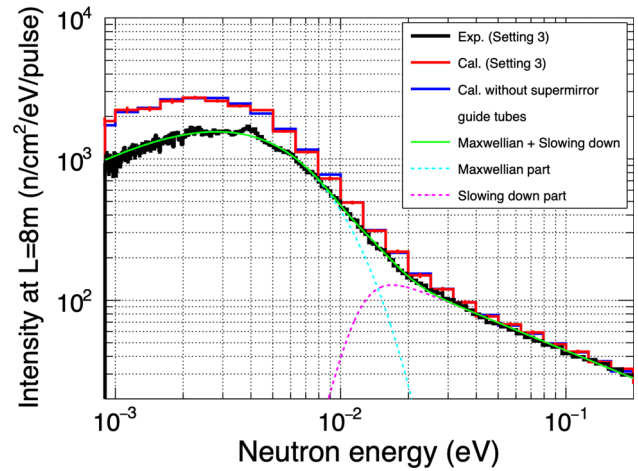
$$R = \begin{cases} R_0 & \text{if } Q \leq Q_c \\ \frac{1}{2} R_0 \left(1 - \tanh \left[\frac{(Q - mQ_c)}{W} \right] \right) (1 - \alpha(Q - Q_c)) & \text{if } Q > Q_c \end{cases} \quad (1)$$

where R is the reflectivity, Q is the absolute value of the scattering vector, Q_c is the absolute value of the critical scattering vector at a Ni layer, and m is the performance value of the supermirror compared to Q_c . The parameter R_0 is the reflectivity at Q less than or equal to Q_c , α is the slope of the reflectivity at Q from Q_c to the cutoff mQ_c , and W is the width of the reflectivity at the cutoff value. The reflectivity functions are shown in Fig. 9, and the numerical values of the parameters m , R_0 , α , and W evaluated from the manufacture’s data are summarized in Table 2. The reflectivity of the first guide tube section at Q larger than Q_c is higher than that of the second and third sections owing to its smaller value of α .

Table 2 Four parameters used in Eq. (1)

Supermirror guide tube section	m	R_0	α (Å)	W (Å ⁻¹)
First	3.15	1.0	2.5	0.0015
Second and third	3.15	1.0	5.0	0.0010

Fig. 10 Comparison of neutron intensity spectra at 8.0 m from the moderator as a function of neutron energy for the experiment and calculation. The experimental spectrum was obtained at setting 3. Two calculated spectra are shown, spectrum for setting 3 (red) and without supermirror guide tube (blue). The solid green curve is the fit result of the experimental spectrum by Eq. (2). The dashed light-blue and pink curves show the Maxwellian and slowing-down parts in Eq. (2)



4 Results and discussions

4.1 Neutron intensity spectra from the moderator

To compare the neutron intensity spectra for the experiment and calculation in absolute values, the calculation data were scaled to the electron beam charge in a single pulse consumed for neutron production in the experiment. The measured charge at the neutron production target in a single pulse was 3.44×10^{-7} C; therefore, the estimated charge available for the neutron production per pulse was 2.57×10^{-7} C, which was obtained by multiplying the measured charge by 0.75, as explained in Sect. 3.5. As explained above, this normalization corresponds to the case where the operating power of the AISTANS electron accelerator is ~1 kW.

Figure 10 shows a comparison of the measured neutron intensity spectrum at 8 m from the moderator as a function of the neutron energy with the simulated spectra from the Monte Carlo simulations. The measured spectrum was obtained by setting 3. The attenuation of neutrons by aluminum materials and air between the moderator surface and neutron detector was considered for the measured spectrum. The simulated spectra for both setting 3 and without supermirror guide tubes were plotted. Both calculation spectra were similar, and the difference was approximately 10% at maximum. Therefore, when analyzing the absolute intensity of the neutron flux spectra just after the emission from the moderator, the experimental data obtained in setting 3 can be used without considering the supermirror guide tube effect. The reason for this is explained in Sect. 4.2.

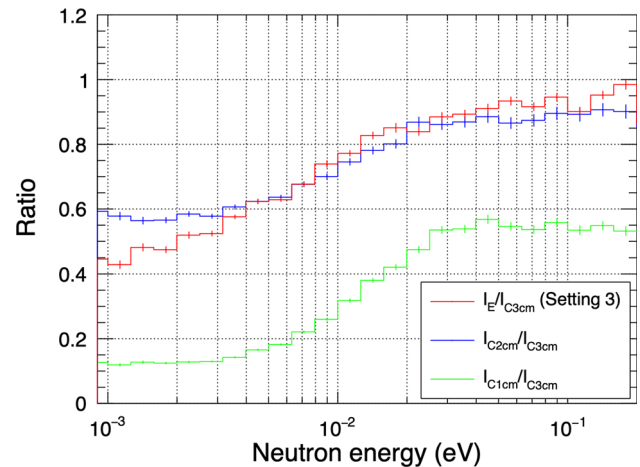
The thermal peaks for both the experimental and calculated spectra were observed at almost the same neutron energy of approximately 3 meV, and this result indicates that the slowing down of neutrons in the solid methane moderator at AISTANS occurred as expected. To evaluate the neutron temperature, the experimental spectrum was fitted by the following equation composed of two components: the Maxwellian thermal equilibrium peak and a neutron slowing-down spectrum, for the neutron energy E [40]:

$$I(E) = I_{Th} \frac{E}{E_T^2} \exp\left(\frac{-E}{E_T}\right) + I_{epi} \frac{1}{E} \Delta(E) \left(\frac{E}{E_0}\right)^\alpha, \tag{2}$$

$$\Delta(E) = \left[1 + \left(\frac{E_{co}}{E}\right)^s\right]^{-1}. \tag{3}$$

Here, I_{Th} and I_{epi} are the thermal and epithermal neutron-beam currents, respectively. In the Maxwellian term, $E_T = k_B T_{eff}$, where k_B is the Boltzmann constant and T_{eff} is the effective temperature of the neutrons. In the slowing-down term, E_0 is the reference energy, which is conventionally taken to be 1 eV. The α term is a constant related to the neutron leakage probability from the moderator. The value $\Delta(E)$ is the smooth cutoff function of the slowing-down spectrum and is given by Eq. (3), where E_{co} and s are free parameters, and E_{co} is the energy at which $\Delta(E) = 1/2$. The fit was performed with the variable E , and the free parameters T_{eff} , I_{Th} , I_{epi} , α , E_{co} , and s . Fitted curves with Eq. (2) are shown in Fig. 10. The obtained effective temperature was 32.6 ± 0.1 K. Typically, the effective temperature of neutrons from a solid methane moderator at a low temperature was higher than the actual moderator temperature [41]. The moderator temperature could be estimated from this effective temperature using the relation derived by Inoue et al. [41]. Using this relation, the moderator temperature was estimated to be 26.2 ± 0.1 K. This value is reasonably close to the base temperature (~20 K) of the cryostat used to produce the solid methane moderator system at AISTANS.

Fig. 11 Ratio of the experimentally measured neutron intensity (I_E) to a calculation (I_{C3cm}) assuming a 3-cm-thick moderator and supermirror guide tubes at setting 3 (red) as a function of neutron energy. Also plotted are the ratio of calculations between different solid-methane thicknesses I_{C2cm}/I_{C3cm} (blue) and I_{C1cm}/I_{C3cm} (green)



The experimentally measured absolute intensity of the neutron beam was of the same order of magnitude when comparing the calculation results over the entire energy region in Fig. 10. The agreement is significantly good in the higher-energy region, although the measured intensity was found to be lower than the calculation as the neutron energy decreased. To discuss the neutron energy dependence of the deviation between the experiment and calculation in detail, the ratio of the experimentally measured intensity to the calculation for setting 3 is shown in Fig. 11 (red line). The ratio approaches one at high energy but decreases toward a value of 0.4, for a neutron energy of 10^{-3} eV. The ratio is $\sim 2/3$ around 5 meV, which corresponds to the wavelength of around 0.4 nm. The wavelength range around 0.4 nm is especially important for the Bragg-edge measurements for analysis of metals such as steel and aluminum.

For comparison, calculations of the neutron intensity assuming 2- and 1-cm-thick solid methane moderators were also performed, and the ratios of these calculated spectra to the original calculation for a 3 cm thick moderator were plotted (blue and green lines). These two calculation results, which modify the moderator thickness, show a similar energy dependence as the ratio between the experiment and calculation at the setting 3. Particularly, the calculation results for the 2-cm-thick solid methane moderator well reproduced the experimental results. This implies that one of the possibilities for the observed difference between the experimental and calculation result is a deficiency in the thickness of the solid methane moderator inside the moderator vessel within an inner dimension of 3 cm. The densities of liquid and solid methane were 0.45 g/cm^3 [42] and 0.52 g/cm^3 [43], respectively. In addition to the difference between these two phases, solid methane is produced by solidification from the surface of the inner walls of the moderator vessel. Furthermore, the thermal conductivity was quite low ($\sim 3 \text{ mW/cm K}$) at 20 K [44]. These conditions may cause internal voids in solid methane during solidification. At the ISIS solid methane moderator, aluminum foam was installed inside the moderator vessel to compensate for low conductivity [45]. The introduction of a similar type of material may be useful for future improvement of AISTANS.

4.2 Performance evaluation of the supermirror guide tubes by geometrical and phase-space methods

In this section, we evaluate qualitatively the neutron transportation performance and effect on measurement images of the supermirror guide tubes without simulation conventionally performed for design and evaluation of a neutron guide system [36]. AISTANS is the first application of the supermirror guide tubes with a thermal-cold neutron source at a CANS for neutron imaging and qualitative knowledge of the neutron transportation is useful for improving or developing other facilities.

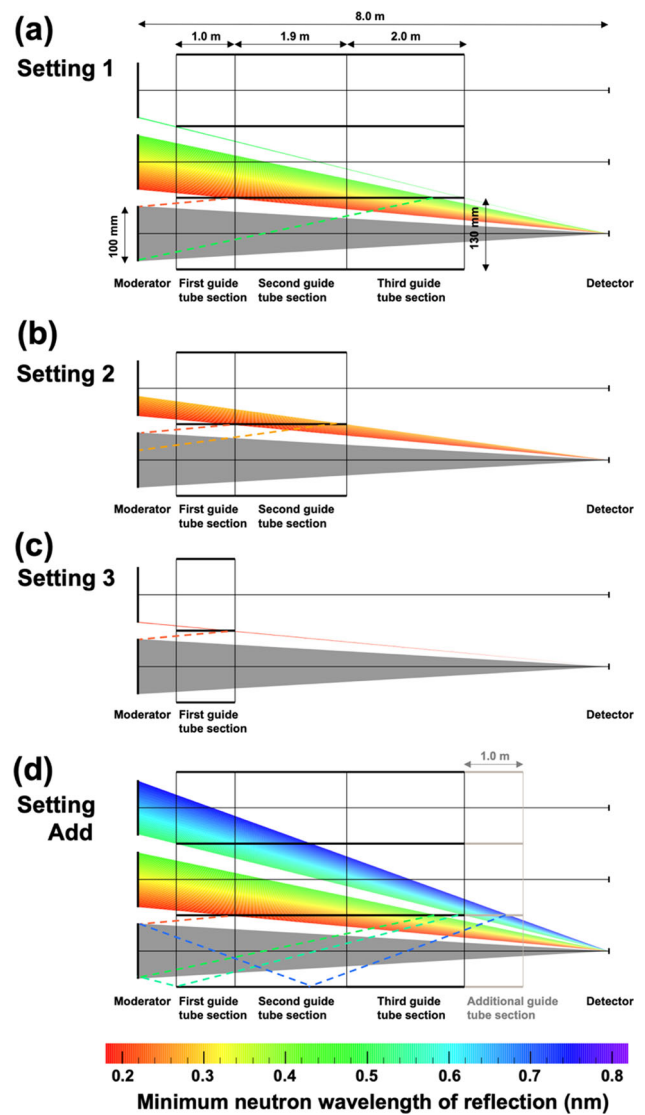
For the qualitative evaluation, first the neutron path through the supermirror guide tubes from the entire region of moderator surface to the center position of the detector position is calculated for each of the three guide tube settings using a geometrical method. Then neutron distributions in the phase space are determined, and the distribution of neutrons arriving at a $100 \times 100 \text{ mm}$ region at the detector position from the entire region of the moderator surface is evaluated.

The two analytical methods, which is based on the neutron optics [46], described in this section allow us to easily estimate the divergence angle of the neutron beam reaching the detector using the supermirror guide tubes. Therefore, it is also possible to evaluate the degree of image blurring of the acquired neutron transmission imaging with/without the supermirror guide tubes.

4.2.1 Analysis by the geometrical neutron path

A geometric analysis of the neutron path in a two-dimensional plane (horizontal or vertical plane) was performed from the moderator to the beamline center at a distance of 8.0 m (= the detector position), as shown in Fig. 12. Figure 12(a), (b), and (c) shows experimental settings 1, 2, and 3, respectively. Figure 12(d) is an additional case assuming setting 1, but adding a 1-m-long supermirror guide tube following the third guide tube section. To simplify the discussion, the inner sizes of all the supermirror guide tubes were assumed to

Fig. 12 Analysis by the neutron path. (a), (b), and (c) represents the experimental settings 1, 2, and 3, respectively. (d) is the case adding a 1-m-long supermirror guide tube followed by the third guide tube section at setting 1. The inner sizes of all supermirror guide tubes were assumed to be 130 × 130 mm and the gaps between the guide tubes were assumed to be zero by lengthening each guide tube. The colored areas are the neutron paths with single or double reflection. The gray areas show the neutron paths reaching the 8-m position directly from the moderators



be 130 mm in width, and the gaps between the guide tubes were assumed to be zero by lengthening each guide tube. The lengths of the first, second, and third guide tube sections were set to be approximately 1.0, 1.9, and 2.0 m, respectively. The neutron reflectivity was assumed to be 100% at Q less than or equal to $3Q_c$. Each of the four diagrams in Fig. 12(a)–(d) shows a representation of the beamline from the moderator to the detector, with the position of the supermirror guide tube sections for each setting superimposed. The shaded grey areas show the possible paths for neutrons to arrive directly at the detector (on the axis at 8.0 m) from the moderator. The dashed lines in each diagram represent the reflected paths. The colored areas are representations of these reflected neutron paths with single or double reflections traced back to the position of the virtual moderator in each case. Colors represent the minimum neutron wavelengths reflected by the supermirror guide tubes. The critical angle of reflection θ_c (in radians) is calculated by the following equation from reference [35]:

$$\theta_c = 0.017 \times m \times \lambda \tag{4}$$

where m is the performance value of the supermirror compared to Q_c and λ is the neutron wavelength in nm.

In the case of setting 3 in Fig. 12(c), only a limited amount of reflection occurred. For setting 2 in Fig. 12(b), there is a single reflection in the minimum neutron wavelength region (0.20–0.28 nm). That is, an amplification effect on the neutron transportation appeared in the range of 0.20–0.28 nm. In setting 1 in Fig. 12(a), a single reflection was dominant, although some double reflections were also possible. The minimum neutron wavelength region of the single reflection was 0.20–0.44 nm. Assuming that the dependence of the neutron emission angle from the moderator on the neutron wavelength is negligibly small, the amplification effect of the neutron transportation by the supermirror guide tubes increases as the wavelength becomes longer in the range of 0.20 to 0.44 nm and saturates at 0.44 nm. With an approximation that the solid angles for a direct viewing of the moderator and indirect

viewings through a single reflection on each inner surface (top, bottom, right, and left) of the supermirror guide tubes from the detector position are equal, an amplification effect of five times can be expected.

Even in setting 1, the first guide tube did not contribute significantly to neutron transportation. However, by adding an additional supermirror guide tube, as shown in Fig. 12(d), a large increase in double reflection becomes possible, and the first guide tubes can be effectively used for this double reflection at longer wavelengths. The neutron transportation effect is sufficiently large at setting 1 for neutron wavelengths around 0.4 nm. However, the additional supermirror guide tube is useful for Bragg edges that have a wavelength much larger than 0.4 nm, for example, those of electrode materials in lithium-ion batteries [47]. By using double reflection, the transportation effect can be extended to wavelengths up to 0.52–0.76 nm. Note that the reflection occurs independently in the horizontal and vertical directions; therefore, the actual number of reflections is twice that shown in Fig. 12.

The image quality (or amount of image blurring) depends on the degree of beam divergence and the distance between the object and neutron detector. In the setting 3, almost no neutron reflection occurs by the supermirror guide tubes. Then, the beam divergence is defined by the neutron emission area (0.1×0.1 m) of the moderator surface and distance between the moderator and neutron detector (~ 8 m) when the 130×130 mm size pinhole was selected. Then, the maximum beam divergence is ~ 12.5 ($= 0.1/8$) mrad for all neutron wavelengths. In the other settings, the neutron reflection occurs by the supermirror guide tubes and the reflection angle is 20.4 mrad for 0.4-nm neutrons from Eq. (4). When the distance between the object and neutron detector is ~ 10 mm, the degree of image blurring for setting 3 and the other settings is ~ 0.13 ($= 10 \times 0.125$) and ~ 0.40 ($= 10 \times 0.0204 \times 2$, here the factor 2 is due to both sides of the supermirror guide tube surfaces) mm, respectively.

4.2.2 Analysis by the neutron phase space

Analysis of the neutron phase space at wavelengths (λ_0) of 0.4 and 0.7 nm was performed from the moderator to the detector position under the same neutron transport conditions as outlined in Sect. 4.2.1 and the results are shown in Fig. 13. The system with an additional guide tube is abbreviated as Add. Neutrons in the phase space in the X direction (horizontal or vertical) between -50 and $+50$ mm and of the wavenumber in the X direction ($k_x = k_0 \times \sin\theta \approx k_0 \times \theta$) from 0 to $+0.4$ nm^{-1} were transported from the moderator position, where the k_0 is the absolute value of the wave vector ($k_0 = 2\pi/\lambda_0$) and θ is the angle between the flight direction of neutrons and the central axis of the beamline. Here, 100% reflection was assumed at the specular reflection condition in which the scattering vector $|2 \times k_x|$ was between 0 and 0.65 nm^{-1} (corresponding to m -value of the supermirror guide tubes from 0 to 3). The results are shown by the phase spaces at five positions in the beamline direction: the moderator surface, exits of the first, second, and third guide tube sections, and the detector position. Figure 13(a) and (b) shows the results for the neutron wavelengths λ_0 of 0.4 and 0.7 nm. The red-colored phase-space neutrons correspond to neutrons with an X -position between -50 and $+50$ mm at the detector position. The neutrons that arrive outside this area are indicated in blue.

As shown in Fig. 13(a), neutrons emitted from the moderator moved in the positive direction on the X axis without changing the wavenumber. When neutrons arrived at the surface of the supermirror guide tube, neutrons with an absolute wavenumber $|k_x|$ less than or equal to 0.32 nm^{-1} were reflected. Neutrons with other wavenumbers were lost. The sign of the wavenumber and direction of movement on the X axis changed by reflection. Then, at the exit of the first guide tube section, the neutrons reflected in this section were recognized in the negative wavenumber area as a small triangular shape for all supermirror guide tube settings. The space gaps in the vertical direction indicated by the double arrow originate from two geometrical reasons: the missing guide tube between the moderator and the first guide tube ($L = 651$ mm) and the wider width of the first guide tube section (130 mm) than that of the moderator (100 mm). The width of the supermirror guide tubes (130 mm) was designed to provide an approximately 100×100 mm field of view at 8.0 m from the moderator [19].

In setting 3 in Fig. 13(a), the number of reflected neutrons at the center of the beamline ($X = 0$ mm) of the detector position was almost zero. This means that the experimental data at setting 3 in this study can be used for diagnosing the 0.4-nm neutrons emitted from the moderator without the effect of the supermirror guide tubes. This conclusion was confirmed to be valid for the entire neutron-wavelength region in the experiment.

The phase-space area of the reflected neutrons in the negative wavenumber region increased as the number of the guide tube sections increased, as recognized in the phase-space diagrams at the detector position in Fig. 13(a). However, double-reflection neutrons, which appear in the positive wavenumber region, do not exist. Therefore, the maximum number of reflections is one at settings 1, 2, and 3, and it is the same even at setting Add for 0.4-nm neutron. Notably, the maximum number of reflections in the two-dimensional (X – Y) space is two because the vertical and horizontal reflections are independent. This result is consistent with that presented in Sect. 4.2.1. At the detector position, there is a discontinuity in wavenumber k_x in the phase space. This implies that a discontinuity in the incident angle θ of the neutrons exists at the detector/sample. In other words, θ depends on the position of the detector/sample. When acquiring a neutron transmission image with high spatial resolution, it should be noted that the blur of the sample image owing to the change in the neutron incident angle may differ depending on the position of the detector/sample.

From the comparison of figures at the moderator surface in Fig. 13(a), the red area of setting 1 is about twice as large as that of setting 3. Assuming that neutrons are emitted from the moderator with a uniform density in the considering phase space, and considering that the actual experimental setup is a two-dimensional (X – Y) system, it implies that the transport efficiency of setting 1 is more than ~ 4 times that of setting 3. It is noticed that the transport efficiency here in Sect. 4.2.2 is related to the neutrons arriving

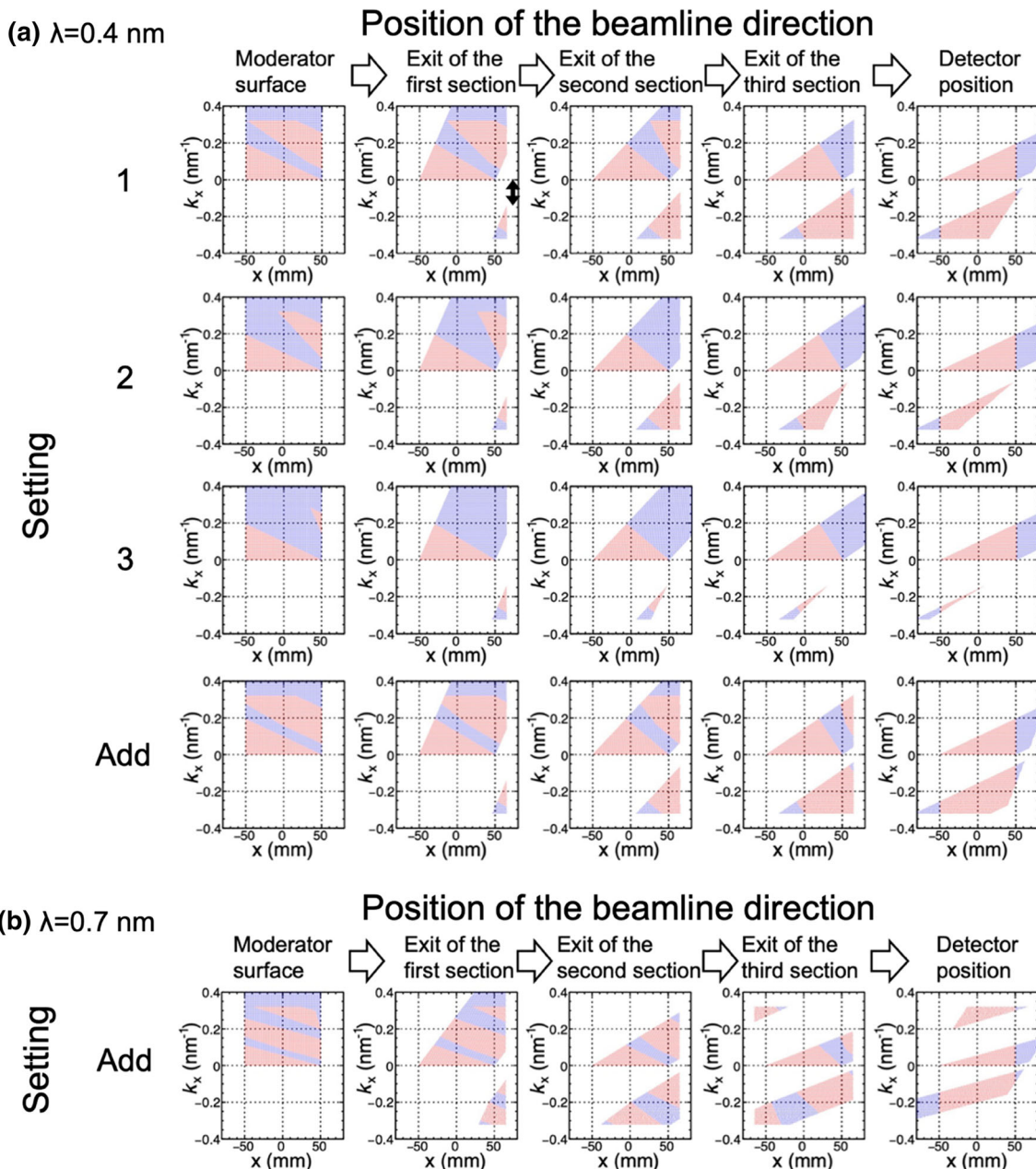
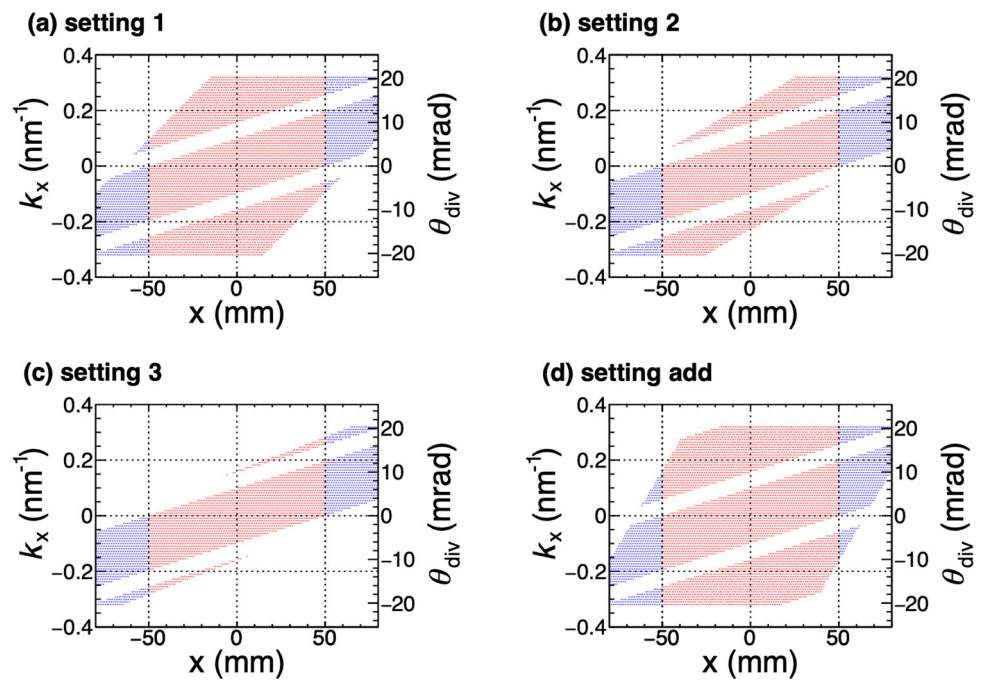


Fig. 13 Analysis of neutron transport by the neutron phase space at 0.4 nm (a) and 0.7 nm (b). Each individual figure shows a plot of the neutron phase space of with the X -axis corresponding to neutron position in the X direction (horizontal or vertical) between -50 and $+50$ mm of the beamline axis, and wavenumber plotted on the Y -axis. In the simulation, neutrons with wavenumber (k_x) from 0 to $+0.4$ nm⁻¹ were transported from the moderator position to the detector. The phase space distributions are shown at the positions of the moderator surface, exits of the first, second, and third guide tube sections, and the detector position. The red-colored phase-space correspond to those neutrons which arrive at the detector position with an X -position between -50 and $+50$ mm. In contrast, the blue-colored phase space corresponds to those neutrons which arrive at the detector position outside this range

at the large area of the detector (100×100 mm). Therefore, it implies that the guide tube is effective for improving the count rate by several times even when measuring the Bragg edge of a relatively large sample with a size close to 100×100 mm.

Figure 13(b) shows the phase spaces for 0.7-nm neutrons at setting Add. The basic movement of 0.7-nm neutrons in the phase space is the same as that of 0.4-nm neutrons. However, the phase space points moved further in the $+x$ or $-x$ direction at the same wavenumber compared to the 0.4-nm neutrons. This is because the speed of $\lambda_0 = 0.7$ nm neutrons in the beamline direction is slower than that of 0.4-nm neutrons. The space gap for the vertical direction at the same position as that discussed in Fig. 13(a) is narrower in the case of 0.7 nm than that of the 0.4 nm. This is related to the larger movement in the $+x$ or $-x$ direction. Contrary to the 0.4-nm neutrons, the second reflection was recognized at the exit of the third guide tube section and the detector position at

Fig. 14 The phase space distributions for 0.4-nm neutrons at the detector position with an initial wavenumber in X -direction from -0.4 to $+0.4 \text{ nm}^{-1}$ at the moderator surface. (a), (b), (c) and (d) represents the phase spaces for settings 1, 2, 3, and add, respectively. The red-colored phase-space correspond to those neutrons which arrive at the detector position with an X -position between -50 and $+50$ mm. In contrast, the blue-colored phase space corresponds to those neutrons which arrive at the detector position outside this range



the wavenumber $k_x \sim 0.3 \text{ nm}^{-1}$. The double reflection phenomenon at 0.7 nm was consistent with the result of the geometrical neutron path analysis, as discussed in Sect. 4.2.1.

Figure 14 shows the phase space for 0.4-nm neutrons at the detector position ($L = 8 \text{ m}$) for each the four settings with an initial wavenumber in X -direction from -0.4 to $+0.4 \text{ nm}^{-1}$ at the moderator surface. In addition, the beam divergence angle (θ_{div}) is added on the right vertical axis. The maximum divergence angles of the beam reaching the detector center ($X \sim 0$) are 40.8 and 12.5 mrad at settings 1 and 3, respectively (see Fig. 14). This result is consistent with that discussed in Sect. 4.2.1 and gives the same image blurring. In addition, Fig. 14 shows difference of the phase-space uniformity depending on the settings, which have effect on the image blurring. The additional setting (add) provides the most spatially symmetric blur in the $100 \times 100 \text{ mm}$ imaging area.

4.3 Quantitative evaluation of the amplification effect of the supermirror guide tubes by comparing experimental data and simulation calculations

Figure 15 shows modified neutron intensity spectra at the sample position as a function of the neutron wavelength for the experimental data and calculations at settings 1, 2, and 3. Note that the experimental spectra in Fig. 15 were obtained by removal of attenuation from aluminum and air from the spectra in Fig. 6 using the attenuation estimation obtained in Sect. 3.4 and these modified spectra can be used to evaluate the amplification factor of the supermirror guide tubes. The vertical axis of the calculations is normalized by the single neutron pulse with the experimental electron beam condition on the target. At a neutron wavelength less than or equal to 0.20 nm , no reflection occurred as explained in Sect. 4.2.1, all three experimental spectra are in good agreement with the calculations. At wavelengths longer than 0.20 nm , there were deviations between the experimental spectra and calculations, and the intensity of the experiments was lower than that of the calculations. This may be owing to the deficiency in the effective thickness of the solid methane moderator, as discussed in Sect. 4.1. The small dips observed at approximately 0.4 nm in all experimental spectra were owing to the incompleteness of the Bragg edge correction for aluminum materials between the moderator and the neutron detector, and the indentation became more emphasized as the neutron flux was increased by the supermirror guide tubes. This feature in the spectra was observed because various types of aluminum materials were used, and their crystalline orientations were more complex to reproduce.

The amplification factors of the neutron flux as a function of wavelength by the supermirror guide tubes are shown in Fig. 16. These factors were calculated as the ratio of neutron flux spectra to that of setting 3, and there was a negligible reflection by the supermirror guide tubes, as discussed in Sects. 4.2.1 and 4.2.2. Amplification factors for settings 1 and 2 raised from one around 0.20 nm and saturated at approximately 0.30 nm and 0.45 nm , respectively. These results agree with the discussion in Sect. 4.2.1. The absolute values of the experimental spectra were in good agreement with the calculations. The amplification factor at setting 1 reached approximately 6 at a wavelength of approximately 0.4 nm and approximately 8 at a wavelength longer than 0.7 nm , demonstrating the effectiveness of the supermirror guide tube. This result is particularly important at a CANS, where the neutron intensity is limited compared to large facilities.

Fig. 15 Neutron intensity, in which the attenuation from aluminum and air including the aluminum moderator vessel are removed, at the sample position as a function of the neutron wavelength for experimental data and calculations at settings 1, 2, and 3. The actual neutron intensity spectra are shown in Fig. 6

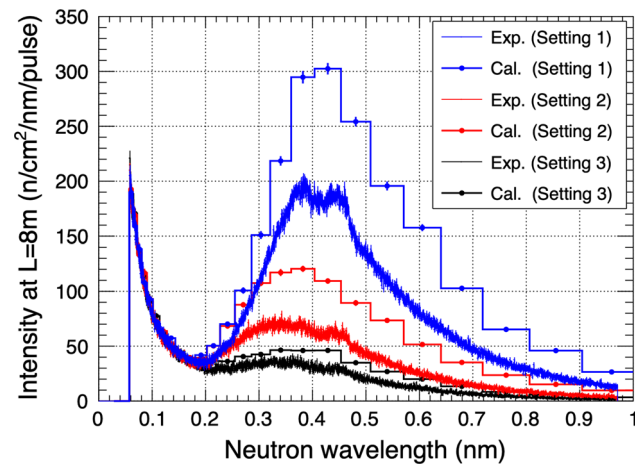
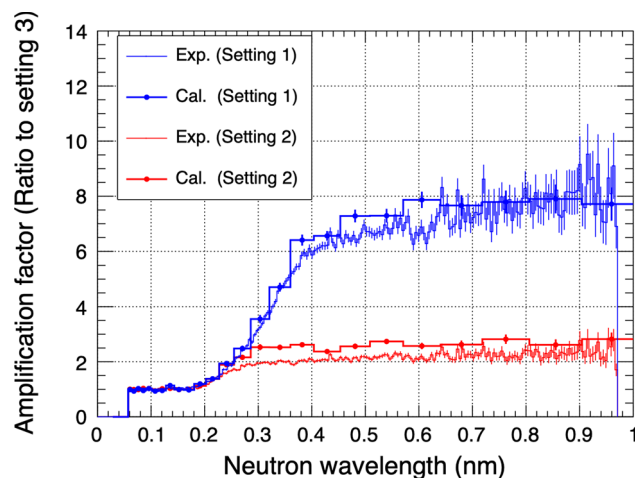


Fig. 16 Amplification factors for the neutron transportation as determined experimentally and from calculations for setting 1 and 2. These factors were obtained by the ratio of neutron flux spectra to that of setting 3



5 Conclusion

We measured the first neutron-beam flux spectra at the compact electron accelerator-driven pulsed neutron facility AISTANS, which was optimized for Bragg-edge imaging, with a neutron transportation system using supermirror guide tubes. The neutron beam, which was produced by irradiation of a ~ 40 MeV electron beam on a Ta target and moderated by a decoupled ~ 20 K solid methane moderator, was detected by a neutron detector at a TOF distance of 8 m for three different settings of the supermirror guide tube configurations.

By fitting the experimentally measured neutron energy spectra with a theoretical function, an effective neutron temperature of 32.6 ± 0.1 K was found. This value implied a moderator temperature of 26.2 ± 0.1 K, close to the ~ 20 K base temperature of the moderator cryostat. The absolute intensity at neutron energies higher than the thermal peak was in good agreement with the simulation calculations. The absolute intensity of the thermal peak of the experimental data was of the same order as that of the calculated spectrum ($\sim 2/3$), and the deviation between the experiment and calculation may be owing to incomplete solidification of the solid methane moderator and subsequent overestimation of the moderator thickness.

The geometrical neutron path and neutron phase space through the supermirror guide tubes were studied diagrammatically. From these analyses, the relationship between the neutron reflection position and wavelength and the effect on the imaging quality (or degree of image blurring) was quantitatively revealed.

The increase in neutron intensity at the detector position when supermirror guide tubes were used, compared to the intensity when not used, the neutron amplification factor, was evaluated by both experimentally and via simulations of the beam transport through the supermirror guide tubes. Large values of the amplification factor were experimentally observed, about 6 at a wavelength of approximately 0.4 nm and about 8 at wavelengths longer than 0.7 nm. These experimental results were well reproduced by the Monte Carlo simulation.

The effective operation of the moderator and supermirror guide tubes has been demonstrated. AISTANS can be used for Bragg-edge imaging of structural materials. The results of this study can be effectively used to improve the efficiency of general experimental measurements with any CANS, not limited to Bragg-edge measurements.

Acknowledgements The new neutron facility is being developed under the auspices of the Innovative Structural Materials Association (ISMA), which is promoting weight reduction in automobiles and other transportation vehicles. This paper is based on results obtained from the ISMA project, JPNP14014, commissioned by the New Energy and Industrial Technology Development Organization (NEDO).

Data Availability Statement This manuscript has associated data in a data repository. [Authors' comment: The datasets generated during and/or analyzed during the current study are available from the corresponding author on reasonable request.]

References

1. H. Takada et al., *Quantum Beam Sci.* **1**, 8 (2017). <https://doi.org/10.3390/qubs1020008>
2. J.R. Haines et al., *Nucl. Instrum. Meth. Phys. Res. Sect. A.* **764**, 94–115 (2014). <https://doi.org/10.1016/j.nima.2014.03.068>
3. J.W.G. Thomason, *Nucl. Instrum. Meth. Phys. Res. Sect. A.* **917**, 61–67 (2019). <https://doi.org/10.1016/j.nima.2018.11.129>
4. H. Chen, X.L. Wang, *Nat. Mater.* **15**, 689–691 (2016). <https://doi.org/10.1038/nmat4655>
5. R. Garoby, *JPS Conf. Proc.* **33**, 011003 (2021). <https://doi.org/10.7566/JPSCP.33.011003>
6. C. Andreani, C.-K. Loong, G. Prete, *Eur. Phys. J. Plus.* **131**, 217 (2016). <https://doi.org/10.1140/epjp/i2016-16217-1>
7. Union for Compact Accelerator-Driven Neutron Sources (UCANS) <http://www.ucans.org>
8. J.R. Granada et al., *Eur. Phys. J. Plus.* **131**, 216 (2016). <https://doi.org/10.1140/epjp/i2016-16216-2>
9. The linear electron accelerator facility in Geel (GELINA). https://joint-research-centre.ec.europa.eu/laboratories-and-facilities/jrc-neutron-time-flight-facility_en
10. X. Wang et al., *J. Phys.: Conf. Ser.* **1021**, 012006 (2018). <https://doi.org/10.1088/1742-6596/1021/1/012006>
11. I. Mardor et al., *Eur. Phys. J. A* **54**, 91 (2018). <https://doi.org/10.1140/epja/i2018-12526-2>
12. G. N. Kim et al., Proceedings of the Second Asian Particle Accelerator Conferences, Beijing, China, (2001). <https://citeseerx.ist.psu.edu/viewdoc/download?doi=10.1.1.554.937&rep=rep1&type=pdf>
13. I.S. Anderson et al., *Phys. Rep.* **654**, 1 (2016). <https://doi.org/10.1016/j.physrep.2016.07.007>
14. <https://nucleus.iaea.org/sites/accelerators/Pages/default.aspx>
15. Y. Kiyanagi, *Eur. Phys. J. Plus.* **131**, 132 (2016). <https://doi.org/10.1140/epjp/i2016-16132-5>
16. Japan Collaboration on Accelerator-Driven Neutron Sources (JCANS). <http://www.jcans.net/index.html>
17. M. Furusaka, H. Sato, T. Kamiyama, M. Ohnuma, Y. Kiyanagi, *Phys. Procedia.* **60**, 167–174 (2014). <https://doi.org/10.1016/j.phpro.2014.11.024>
18. Y. Otake, *Plasma Fusion Res.* **13**, 2401017 (2018). <https://doi.org/10.1585/pfr.13.2401017>
19. K. Kino et al., *Nucl. Instrum. Meth. Phys. Res. Sect. A.* **927**, 407–418 (2019). <https://doi.org/10.1016/j.nima.2019.02.062>
20. B.E. O'Rourke et al., *Nucl. Instrum. Meth. Phys. Res. Sect. B.* **464**, 41–44 (2020). <https://doi.org/10.1016/j.nimb.2019.11.041>
21. P. Zakalek et al., *J. Phys. Conf. Ser.* **1401**, 012010 (2020). <https://doi.org/10.1088/1742-6596/1401/1/012010>
22. T. Brückel, T. Gutberlet, eds., Conceptual Design Report Jülich High Brilliance Neutron Source (HBS) https://www.fz-juelich.de/SharedDocs/Downloads/JCNS/JCNS-2/EN/Conceptual-Design-Report-HBS.pdf?__blob=publicationFile
23. U. Rucker et al., *Eur. Phys. J. Plus.* **131**, 19 (2016). <https://doi.org/10.1140/epjp/i2016-16019-5>
24. F. Ott, A. Menelle, C. Alba-Simionesco, *EPJ Web Conf.* **231**, 01004 (2020). <https://doi.org/10.1051/epjconf/202023101004>
25. Y. Kiyanagi, H. Sato, T. Kamiyama, T. Shinohara, *J. Phys. Conf. Ser.* **340**, 012010 (2012). <https://doi.org/10.1088/1742-6596/340/1/012010>
26. R. Woracek, J. Santisteban, A. Fedrigo, M. Strobl, *Nucl. Instrum. Methods Phys. Res. Sect. A* **878**, 141–158 (2018). <https://doi.org/10.1016/j.nima.2017.07.040>
27. T. Shinohara et al., *Rev. Sci. Instrum.* **91**, 043302 (2020). <https://doi.org/10.1063/1.5136034>
28. H. Bilheux, K. Herwig, S. Keener, L. Davis, *Phys. Procedia.* **69**, 55–59 (2015). <https://doi.org/10.1016/j.phpro.2015.07.007>
29. T. Minniti, K. Watanabe, G. Burca, D.E. Pooley, W. Kockelmann, *Nucl. Instrum. Methods Phys. Res. Sect. A* **888**, 184–195 (2018). <https://doi.org/10.1016/j.nima.2018.01.037>
30. M. Strobl, *Phys. Procedia.* **69**, 18–26 (2015). <https://doi.org/10.1016/j.phpro.2015.07.002>
31. <https://europenspallationsource.se/instruments/odin#instrument-description>
32. L. Zanini et al., *Nucl. Instrum. Meth. Phys. Res. Sect. A.* **925**, 33–52 (2019). <https://doi.org/10.1016/j.nima.2019.01.003>
33. H. Sato, Y. Shiota, T. Kamiyama, M. Ohnuma, M. Furusaka, Y. Kiyanagi, *Phys. Procedia.* **60**, 254–263 (2014). <https://doi.org/10.1016/j.phpro.2014.11.035>
34. H. Sato, T. Sasaki, T. Moriya, H. Ishikawa, T. Kamiyama, M. Furusaka, *Phys. B.* **551**, 452–459 (2018). <https://doi.org/10.1016/j.physb.2017.12.058>
35. F. Cousin, A. Menelle, *EPJ Web Conf.* **104**, 01005 (2015). <https://doi.org/10.1051/epjconf/201510401005>
36. Z. Ma, K. Lieutenant, J. Voigt, T. Gutberlet, M. Feygenson, T. Brückel, *Nucl. Instrum. Methods Phys. Res. Sect. A* **1009**, 165479 (2021). <https://doi.org/10.1016/j.nima.2021.165479>
37. H. Sato, T. Kamiyama, Y. Kiyanagi, *Mater. Trans.* **52**, 1294–1302 (2011). <https://doi.org/10.2320/matertrans.M2010328>
38. K. Shibata et al., *J. Nucl. Sci. Technol.* **48**, 1–30 (2011). <https://doi.org/10.1080/18811248.2011.9711675>
39. T. Sato et al., *J. Nucl. Sci. Technol.* **55**, 684–690 (2018). <https://doi.org/10.1080/00223131.2017.1419890>
40. J.M. Carpenter, W.B. Yelon, *Meth. Experim. Phys.* **99**, 99–196 (1986). [https://doi.org/10.1016/S0076-695X\(08\)60555-4](https://doi.org/10.1016/S0076-695X(08)60555-4)
41. K. Inoue, Y. Kiyanagi, H. Iwasa, *Nucl. Instrum. Meth.* **192**, 129–136 (1982). [https://doi.org/10.1016/0029-554X\(82\)90814-X](https://doi.org/10.1016/0029-554X(82)90814-X)
42. D.G. Friend, J.F. Ely, H. Ingham, *J. Phys. Chem. Ref. Data.* **18**, 583–638 (1989). <https://doi.org/10.1063/1.555828>
43. W.H. Ramsey, *Mon. Not. R. Astron. Soc.* **125**, 469–485 (1962). <https://doi.org/10.1093/mnras/125.5.469>
44. A. Jez-dotowski, H. Misiorek, V.V. Sumarokov, B.Y. Gorodilov, *Phys. Rev. B.* **55**, 5578–5580 (1997). <https://doi.org/10.1103/PhysRevB.55.5578>
45. O. Kirichek, C.R. Lawson, D.M. Jenkins, C.J.T. Ridley, D.J. Haynes, *Cryogenics* **88**, 101–105 (2017). <https://doi.org/10.1016/j.cryogenics.2017.10.017>
46. K. Kino et al., *Appl. Phys. Express.* **15**, 027005 (2022). <https://doi.org/10.35848/1882-0786/ac4c45>
47. A.G., Klein, S.A., Werner, *Neutron optics. Rep. Prog. Phys.* **46**(3):259–335 (1983). <https://doi.org/10.1088/0034-4885/46/3/001>

Springer Nature or its licensor (e.g. a society or other partner) holds exclusive rights to this article under a publishing agreement with the author(s) or other rightsholder(s); author self-archiving of the accepted manuscript version of this article is solely governed by the terms of such publishing agreement and applicable law.